Crystallization Behavior of the Hydrogen Sulfide Hydrate Formed in Microcapillaries

Jiyue Sun, I-Ming Chou, Lei Jiang,* Juezhi Lin, and Rui Sun

ACCESS | Metrics & More | Article Recommendations | Supporting Information

ABSTRACT: There are no reports on the hydrogen sulfide hydrate growth process and morphology in micropores due to the toxicity of hydrogen sulfide. In this study, the experimental measurements and dissociation enthalpies were provided to assess the effect of the microcapillary silica tube size on hydrogen sulfide hydrate dissociation conditions. To simulate micropore sediments, the H_2S hydrate growth processes and morphologies at different supercooling temperatures were observed in this study. The dissociation temperature depression of the hydrate crystal in the

microcapillary was less than 0.001 °C, which shows that the stability of the hydrate is less affected by the microcapillary pore used in this study. The mass transfer from the gas phase to the liquid phase is easily blocked when the hydrogen sulfide hydrate shell covers the gas–water meniscus, causing the growth of the gas hydrate to be inhibited. The hydrate crystal morphology can be divided into fibrous, needle-like crystals and dendritic crystals when $\Delta T_{sub} > 12.7$; the hydrate crystal morphology can be categorized as dendritic crystals and columnar crystals when $\Delta T_{sub} = 7.9–8.9$, and the hydrate crystals can form polyhedral crystals when $\Delta T_{sub} = 7.9–8.9$. Additionally, a new "bridging effect" that a hollow crystal which was filled with the gas phase can connect with two separated gas phases was found at low supercooling temperature.
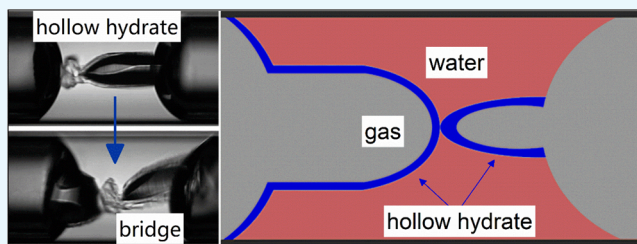
1. INTRODUCTION

Gas hydrates are ice-like, nonstoichiometric compounds formed from water and gas molecules (e.g., CH_4, CO_2, and H_2S) at low temperatures and high pressures. Stable hydrates form when the gas molecules are trapped in the cages built by the water molecules. Different types of cages are built by hydrogen bonding.[1] The main hydrate forms are sI, sII, and sH.[1] Under low-temperature, high-pressure conditions, gas hydrates easily form in gas transmission pipelines, blocking the pipelines and corroding the equipment. As these problems disrupt the normal operation of the oil- and gas-extraction and transportation equipment, preventing the formation of gas hydrates is an urgent priority in oil and gas production and pipeline transmission.[1,2] Gas hydrates are characterized by high gas-storage properties, high thermal properties of generation/ decomposition, and selectivity for guest molecules. These properties have been exploited in various hydrate technologies, such as transportation and storage of natural gas,[3] gas separation,[4] and heat pump/cooling based on the high generation/decomposition heat of hydrates.[5]

Understanding the crystalline morphological characteristics of hydrates is essential for developing hydrate technologies. For example, the crystalline morphology and particle size distribution affect the fluid properties of hydrate slurry. Studies have shown that the slurry hydrate strongly resists flow in pipelines, whereas the powder hydrate consumes less energy and has lower flow resistance, so is suitable for pipeline transport.[6] However, the hydrate crystallization morphology

and growth rate depend on the thermodynamic conditions of hydrate formation, such as the degree of supercooling (ΔT_{sub}), calculated as the difference between the phase-equilibrium temperature T_{eq} and the experimental temperature T_{ex} (i.e., $\Delta T_{sub} = T_{eq} - T_{ex}$). As the degree of supercooling increases, the number of hydrate crystals enlarges and the crystals become smaller; conversely, a smaller supercooling degree results in fewer but larger crystals.[7] Therefore, the supercooling degree can be designed to regulate the formation characteristics of hydrates.

Natural geological sediments possess complex surfaces and porosities. The surface properties and porosity of solid matrices can affect the formation of natural gas hydrates.[8−11] Beltrán and Servio[8] observed that hydrates formed on slides can grow beyond the original water boundary and that hydrate halos can diffuse by forming "bridges" between nucleated and non-nucleated droplets. Nguyen et al.[10] found that the CO_2 gas hydrate forms more readily on hydrophobic glass surfaces than on hydrophilic surfaces. Park et al.[12] showed that the pore size distribution in fine-grained sediments affects the dissociation

temperature of gas hydrates. They also found that the smaller the pore size of the silica gel, the lower is the dissociation temperature of the CO_2 hydrate in the gel.

In many solid matrices, the hydrate formation process is not directly observed but is inferred from macroscopic measurements such as gas consumption.[13,14] In addition, gas hydrate formation processes are usually studied on large substrates (on the milli- and centiscale).[15,16] Relatively few studies have reported the formation of gas hydrates on micron-scale pore substrates, which better simulate the pore characteristics of geological sediments. Touil et al.[17] observed the formation and growth of CO_2 hydrates around water−gas bending surfaces in micron-scale thin capillary silica tubes. They explored the effects of supercooling and mass wettability on hydrate formation but concluded that owing to the paucity of studies conducted under similar or related experimental conditions (e.g., thin glass capillaries and pore networks in depositional matrices), their results could not be compared with the existing results. As we all know, H_2S is an important component of natural gas, but its toxicity has prevented studies on the H_2S hydrate-formation process. From the authors' knowledge, we have not found the report on the hydrogen sulfide hydrate growth process and morphology. The hydrogen sulfide hydrate crystal growth behavior and appearance in the capillary silica tube were observed in this study. The results are helpful to understand the formation, growth, and morphology of gas hydrates in sediment pores.

2. RESULTS AND DISCUSSION

2.1. Raman Spectroscopic Measurement of the H_2S Hydrate.

As shown in Figure 1a, the Raman spectral peaks of different H_2S phases were detected at $T_{ex} = −5$ °C (experiment 1-1). The Raman shifts at 2578, 2611, and 2590 cm^{-1} were attributed to S−H stretching vibrations of liquid-phase H_2S,

gas-phase H_2S, and dissolved H_2S, respectively. After hydrate formation and a temperature increase to $T_{ex} = −5$ °C (Figure 1b), two Raman shifts of H_2S hydrate were detected. The peaks at 2604 and 2593 cm^{-1} were assigned to S−H stretching vibrations of H_2S in the small cage (5^{12}) and large cage ($5^{12}6^2$) of the H_2S hydrate, respectively. These results agree with those of previous reports.[18−20]

2.2. Effect of the Microcapillary Silica Tube Size on H_2S Hydrate Dissociation Conditions.

The limitation of the pore size, especially nanoscale pores, will inhibit the phase equilibrium conditions of gas−water systems.[21,22] However, there is a discrepancy in whether microcapillary silica tubes can inhibit the formation of hydrates. Sun et al.[23] observed that the equilibrium conditions of the ethane hydrate in two different sizes of microcapillaries (500 μm ID and 1000 μm ID) were lower than in the bulk liquid (macroreactor) at the same pressure, where the maximum difference of equilibrium temperature is up to 1.6 °C. However, Touil et al.[17] and Martinez de Baños et al.[24] have measured the three-phase equilibrium temperature of the CO_2 hydrate and cyclopentane hydrate in the capillary silica tube (200 μm ID and 250 μm ID, respectively), and their measurements are in accordance with previous studies.[1,25] As shown in Figure 1, we have measured the H_2S hydrate in the presence of liquid water and liquid hydrogen sulfide, and the measurements were in agreement with our previous study and literature studies.[26,27]

When the temperature and pressure are controlled, the Gibbs free energy is the thermodynamic variable of the phase transition.[28,29] The Gibbs free energy is affected by the surface curvature at the gas−water meniscus in the microcapillary tube, which is affected by capillary pressure.[30] The change in Gibbs free energy can be expressed by the Gibbs−Duhem equation.

$$dG = -S\,dT + V\,dP + \sigma\,dA + \sum \mu_i\,dn_i \quad (1)$$

where S, V, and $\sigma\,dA$ are the entropy, volume, and surface energy, respectively. In addition, the change in Gibbs free energy also can be given by the Gibbs−Helmholtz equation

$$\left(\frac{\partial \Delta G/T}{\partial T}\right) = -\frac{\Delta H}{T^2} \quad (2)$$

where ΔH is the dissociation enthalpy of the gas hydrate which is given in Table 1.

The Gibbs equation makes some thermodynamic substitutions to derive the Gibbs−Thomson equation,[30] which describes the change in dissociation pressure depression of the
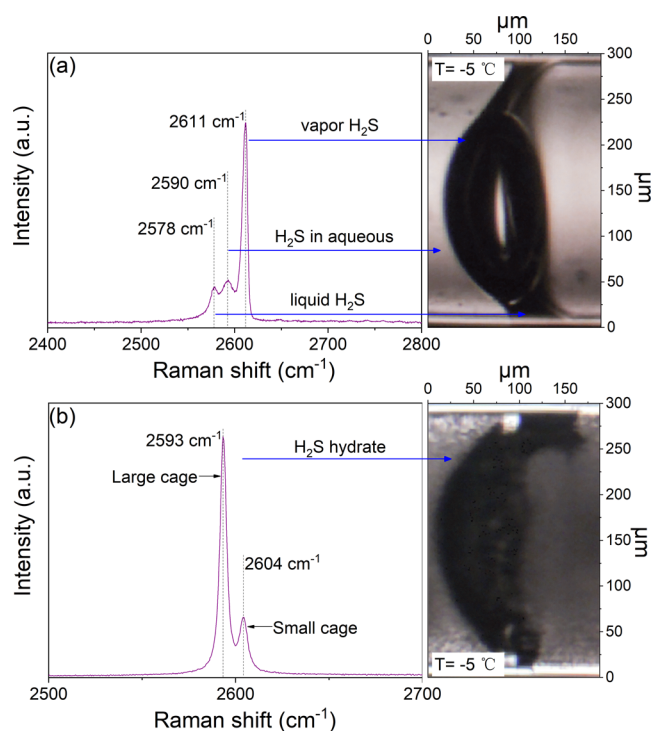

Figure 1. Raman spectra of different phases of H_2S (a) and the H_2S hydrate (b) at $P = 247.6$ psi and $T_{ex} = −5$ °C.

Table 1. Measurements and Dissociation Enthalpies of the H_2S Hydrate along the H−Lw−V Phase Boundary

T_{eq} (°C)	P (psi)	ΔH_f (kJ/g)	$\dfrac{\partial \Delta G(T)}{\partial T}$	pore size (μm)	ΔT_m (°C)
3.2	18.9	73.1	0.00096	100	9.48×10^{-4}
7.4	29.5	72.6	0.00092		9.68×10^{-4}
13.4	54.1	71.5	0.00087		1.01×10^{-3}
18.3	90.5	69.9	0.00082		1.04×10^{-3}
22.0	135.6	67.9	0.00078		1.09×10^{-3}
24.3	178.6	66.2	0.00075		1.13×10^{-3}
26.3	219.5	64.2	0.00072		1.17×10^{-3}
29.6^a	322.9				

^{a}The temperature is out of the H−Lw−V phase boundary.

gas hydrate crystal with the surface curvature. According to the Gibbs−Thomson equation, the dissociation temperature depression (ΔT_m) of the hydrate crystal in pore solids can be expressed below

$$\Delta T_m = T_m^\infty - T_m(x) = \frac{4\sigma_{HW} T_m^\infty}{x \Delta H \rho_s} \cos \phi \qquad (3)$$

where T_m^∞ is the hydrate dissociation temperature in bulk liquid, $T_m(x)$ is the hydrate dissociation temperature in pore solids, σ_{HW} is the surface tension between the hydrate and liquid, and $\sigma_{HW} = 0.0314$ J/m^2, which was taken from Duan et al.[31] ρ_s is the hydrate density, $\rho_s = 1.046$ g/cm^3, which was taken from Carroll,[32] ϕ is the contact angle and assumed to be $\cos \phi = 1$, x is assumed to be 5 nm, 50 nm, 500 nm, 10 μm, 100 μm, and 300 μm in this study, and ΔH is the hydrate dissociation enthalpy which can be calculated from the Clausius−Clapeyron equation

$$\frac{d \ln(P)}{d(1/T)} = \frac{\Delta H}{z_{H_2S} R} \qquad (4)$$

where z_{H_2S} is the compressibility factor of hydrogen sulfide, which was calculated from Duan et al.[33] d ln(P)/d$(1/T)$ can be obtained by fitting measurements in this study. As shown in Table 1, we can see that the dissociation temperatures depression of the hydrate crystal in the microcapillary was less than 0.001 °C, which is less than the measurement error of the thermocouple in the heating and cooling stage. Therefore, the equilibrium measurements of gas hydrates in the microcapillary used in this study are reliable. In fact, when the pore size of the capillary silica tube is less than 0.05 μm, the phase equilibrium conditions of hydrates will be greatly affected $(\Delta T_m > 1 \ °C)$. The porous media will cause extra strain of the hydrate lattice when the pore size is less than 0.05 μm.[34]

2.3. Hydrogen Sulfide Hydrate Growth Process and Morphology.

According to the authors' knowledge, there is no report on the hydrogen sulfide hydrate growth process and morphology. In this study, we reported the hydrogen sulfide hydrate growth process and morphology under different supercooling conditions. The supercooling temperature (ΔT_{sub}) is the difference between the phase-equilibrium temperature T_{eq} and the experimental temperature T_{ex}, which is the isobaric extension from phase equilibrium temperature to nucleation temperature, as shown in Figure 2.

2.3.1. Strong Supercooling Conditions.

The strong super-cooling experiments included experiment 2-1, experiment 4-1, and experiment 4-2, and the cooling rate of all three experiments was 5 or 10 °C/min. Figure 3 shows the formation of the H$_2$S hydrate at T_{eq} = 18.3 °C, ΔT_{sub} = 31.3 °C, and P = 90.5 psi (experiment 2-1). First, the H$_2$S hydrate halo formed at the gas−water interface and expanded rapidly into the water-rich phase, and the growth rate of this halo was 840 μm/s. The hydrate was a microcrystal invisible to the naked eye (Figure 3a). Then, the hydrate crystals gradually coarsened and were clarified under the Ostwald ripening effect over a period of time (Figure 3b). Next, the hydrate halo at the gas−liquid meniscus crept toward the gas-rich side, forming a thin hydrate film (Figure 3b,c), the morphology of the hydrate film evolved from fuzzy to clear, and tiny polyhedral crystals were formed. The growth mechanism of the hydrate film can be explained that the liquid water inside the hydrate film is
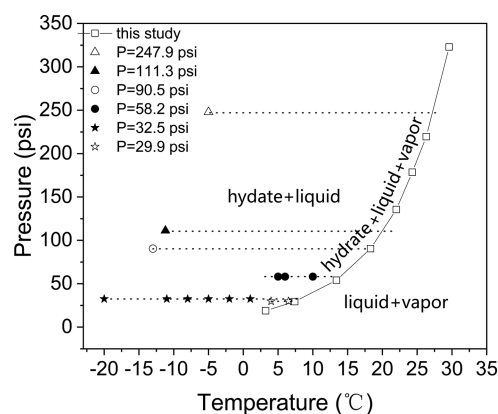

Figure 2. Isobaric extensions from phase equilibrium temperature to nucleation temperature (horizontal dashed lines).

pumped up through the pore spaces between the small hydrate crystals under the capillary force. If the contact between the water and gas molecules is maintained, it may help us to allow the hydrate film to continually grow. However, after the hydrate film grows hundreds of microns in the microcapillary tube, its growth will gradually stop. The possible reason is that the hydrate film cannot continue to thicken due to the formation of a large number of hydrates in the liquid and on the surface of the gas−water meniscus, resulting in blocked mass transfer channels.

Raman spectroscopy can be used to monitor the growth and thickening process of gas hydrate films.[35] As shown in Figure 3d, the peaks at 2593 and 2604 cm^{-1} represent the large-cage and small-cage H$_2$S hydrate structures at focus A in Figure 3b, respectively, and no ice was found. The intensity ratios are close to 3.0, indicating that the hydrate at focus A is an sI H$_2$S hydrate film without free gas interference. In addition, H$_2$S hydrate Raman spectroscopy at focus B in Figure 3d is shown in accordance with focus A. As shown in Figure 3c, we can observe some coarse-grained hydrate crystals on the hydrate film. Furthermore, the Raman shift of 2613 cm^{-1} in Figure 3e, which is the S−H stretching vibrations of the H$_2$S gas molecule and indicated that the hydrate film at point C was interfered with the gas phase, is corresponding to focus C in Figure 3c. It shows that the thickness of the hydrate film in the microcapillary is thin and indicates that the hydrated crust film is porous.

As shown in Figure 4a, the H$_2$S hydrate formed at the gas−water meniscus in fibrous appearance for experiment 4-1 (T_{eq} = 7.7 °C and P = 32.5 psi), where the crystal growth rate exceeded 450 μm/s, and then expanded radially into the solution at ΔT_{sub} = 18.7 °C. A similar CO$_2$ hydrate crystal appearance was reported in the literature.[17] As given in Figure 4b, the H$_2$S hydrate crystals showed a needle-like form and the crystal growth rate exceeded 281 μm/s at ΔT_{sub} = 12.7 °C in experiment 4-2 (T_{eq} = 7.7 °C and P = 32.5 psi). In addition, we also found that the hydrate can crystallize in the dendritic form under strong supercooling conditions (see Video S1). Such needle-like and dendritic crystalline morphologies of hydrates under strong supercooling conditions have been reported by previous studies.[16,36]

2.3.2. Moderate Supercooling Conditions.

The hydrate crystal growth at the interface of gas−liquid is a common phenomenon. We also observed the growth of the hydrate in columnar crystals at the interface between H$_2$S and aqueous
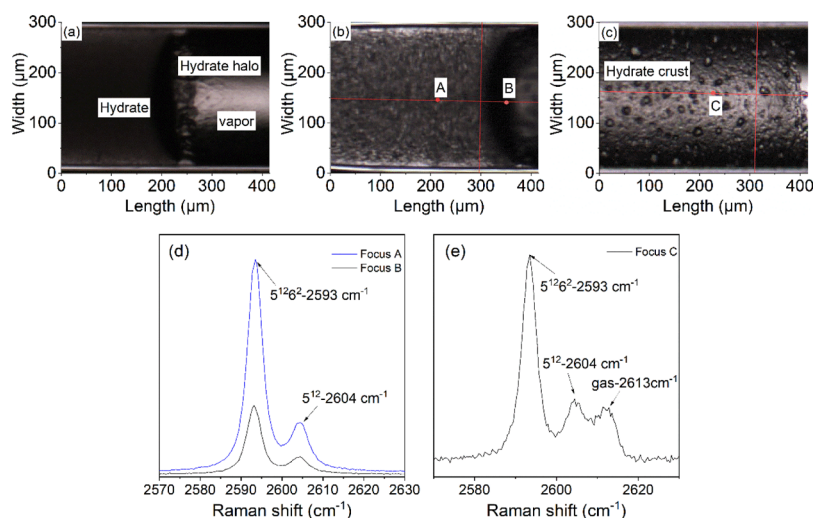
Figure 3. Representative optical microscopy images and Raman spectra of the H$_2$S hydrate film growth process (ΔT_{sub} = 31.3 °C). (a) Initial formation of hydrates; (b) coarsening of hydrate crystal particles; (c) hydrate halo growth; and (d,e) hydrate and H$_2$S vapor Raman spectra.
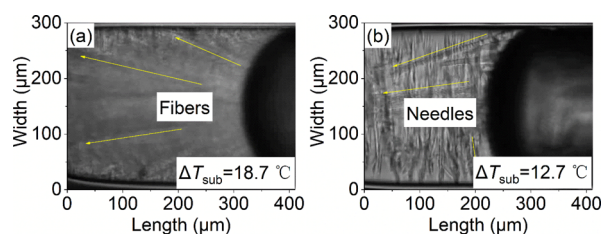

Figure 4. Formation of fibrous (a) crystals at ΔT_{sub} = 18.7 °C and needle-like (b) crystals in microcapillary silica tubes at ΔT_{sub} = 12.7 °C.

solutions under moderate supercooling conditions in experiment 3-1. As shown in Figure 5b, the hydrogen sulfide hydrate was formed at the gas−liquid meniscus, and it was covered with a hydrate crust within 3 s. Next, the mass transfer channel from gas to solution will be blocked since the solubility of gas
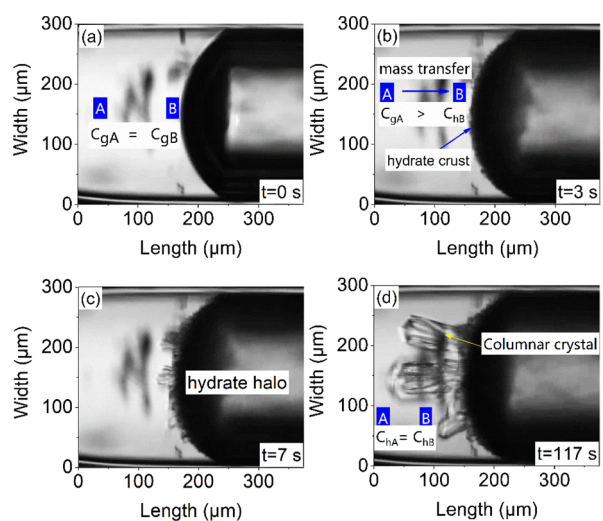

Figure 5. Columnar polyhedral hydrate crystals formed on the liquid surface of the gas−water meniscus at ΔT_{sub} = 8.9 °C: (a) unnucleated images; (b) hydrate nucleation at the gas−water meniscus; (c) hydrate growth from the gas−water meniscus; and (d) columnar polyhedral crystal.

in aqueous solutions without gas hydrates is different from that of gas in aqueous solutions with gas hydrates. According to the mechanism of mass transfer,[37] when the hydrogen sulfide hydrate is not formed, the concentration at point A is equal to the concentration at point B, $C_{gA} = C_{gB}$, as shown in Figure 5a. When the hydrogen sulfide hydrate is formed, the concentration at point A is greater than that at point B, $C_{gA} > C_{hB}$, resulting in a concentration difference that allows the dissolved hydrogen sulfide at point A to diffuse to point B, thus promoting the growth of hydrate crystals from the hydrate film in the meniscus toward bulk of the liquid water, as shown in Figure 5b,c. When the concentration at point A is in accordance with the concentration at point B, $C_{hA} = C_{hB}$, the hydrogen sulfide hydrate will no longer grow, as given in Figure 5d. In addition, the formation of different columnar crystals in Figure 5d may be due to the different surface roughnesses of the hydrate crust in Figure 5b.

On the other hand, when the ΔT_{sub} was equal to 7.9 °C, we observed a phenomenon in experiment 3-2 that the hydrogen sulfide hydrate formed at the substrate of the microcapillary, which can be seen in Video S2. According to Kvamme et al.,[34] the mineral surface will have a water molecule adsorption layer and water on substrate surfaces is structurally close to liquid water. In addition, H$_2$S will be able to compete with water for some direct adsorption on the mineral surface, which makes it possible for H$_2$S hydrates to nucleate in water molecules on substrate surfaces. As shown in Figure 6b,c, after the hydrogen sulfide hydrate forms on the substrate, the hydrate then grows in two different directions in the form of a "zigzag crystal" and the growth rate was estimated at 113 μm/s. As shown in Figure 6d, when the hydrogen sulfide hydrate reaches the gas−water meniscus, it will quickly form a hydrated crust, causing the mass transfer from the gas phase to the liquid phase to be blocked. In addition, there are a lot of raised cellular structures on the "zigzag crystal" form. Moreover, the surplus gas that dissolved in water can promote the secondary side branches of the like-dendrite crystal evolved from the raised cellular structure. According to the mechanism of mass transfer,[37] the surplus gas dissolved in water can promote the raised cellular structure to evolve into the like-dendrite crystal which is a secondary side branch of the "zigzag crystal" form, as shown in Figure 6d.
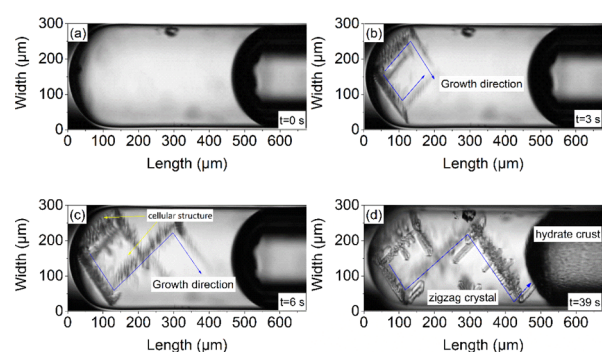
Figure 6. Zigzag crystal growing in the substrate of the silica tube at ΔT_{sub} = 7.9 °C: (a) unnucleated images; (b) hydrate formation at the substrate of the silica tube; (c) hydrate growth in a zigzag form; and (d) hydrate crust formation at the gas−water interface.

2.3.3. Low Supercooling Conditions. To the authors' knowledge, there are only a few studies that report the formation and morphology of the hydrate in microscale pores.[17,38,39] As shown in Figure 7, we observed in this study the radiation growth of floating gas hydrates in aqueous solutions at ΔT_{sub} = 3.9 °C (experiment 3-3), and its growth rate was close to 3.1 μm/s. As shown in Figure 7b,c, the hydrates grow in different directions and form radial polyhedral crystal clusters due to the presence of concentration differences. On the other hand, a variety of floating polyhedral crystals in this study were observed under the low supercooling conditions at ΔT_{sub} < 1.0 °C (experiment 6-1) and ΔT_{sub} = 0.6 °C (experiment 6-2). As given in Figure 8, possible crystal morphologies observed in this study include the polyhedral crystal (Figure 8a), cubic crystal (Figure 8b), and hexagonal crystal (Figure 8c).

We reported the hydrogen sulfide hydrate growth process and morphology under different supercooling conditions in this study. The hydrate crystal morphology can be divided into fibrous, needle-like crystals and dendritic crystals when ΔT_{sub} > 12.7; the hydrate crystal morphology can be categorized as dendritic crystals and columnar crystals when ΔT_{sub} = 7.9−8.9, and the hydrate crystals can form polyhedral crystals when ΔT_{sub} = 7.9−8.9. What is more, the growth of hydrate crystals is affected by mass transfer. When the hydrogen sulfide hydrate reaches the gas−water meniscus, it will quickly form a hydrated crust, causing the mass transfer from the gas phase to the liquid phase being blocked, so that the growth of the gas hydrate was inhibited.

2.4. Bridging Effect in the Microcapillary Silica Tube. So far, a variety of "hydrate bridge" effects have been reported in previous literature studies.[8,23] Beltrán and Servio[8] first found that the hydrate can diffuse between separated droplets by a bridging effect that causes hydrate formation in both nucleated

and non-nucleated droplets. Sun et al.[23] observed the ethane hydrate formation, which is regard as a bridge, between the adjacent bubbles in aqueous solutions. In this study, we observed that the gas hydrates under low supercooling conditions in the microcapillary can provide a bridging function that connects with two separated gas phases in a hollow crystal form, as shown in Figure 9. The growth process of the hollow crystal in the microcapillary tube is provided in Video S3.

We conducted experiment 5-1 (T_{eq} = 7.0 °C and P = 29.9 psi) under low supercooling temperature conditions, ΔT_{sub} = 3.9 °C. As shown in Figure 9a, the floating hydrogen sulfide hydrate crystal of the gas−water meniscus in the microcapillary silica tube was obtained by repeated heating and cooling operations. As shown in Figure 9b, the gas hydrate in the conical crystal form starts from the gas−water meniscus to grow toward the liquid phase under the driving force, and the growth rate is close to 1.7 μm/s. As shown in Figure 9c,d, it is noteworthy that the hydrogen sulfide hydrate during the growth process is not in the solid crystal but in the hollow crystal. The highlighted line in Figure 9 can be determined as the boundary of the hydrate crystal, and the conical hydrate crystal was gradually evolved into cylindrical hollow crystals. In addition, the shaded portion surrounded by the highlighted lines is consistent with the optical phenomenon of the gas-phase hydrogen sulfide on the right side. Touil et al.[17] demonstrated using Raman spectroscopy that the hollow hydrate crystal was filled with the gas phase. Karanjkar et al.[40] found that the cyclopentane hydrate can grow in a hollow conical crystal form from the cyclopentane−water interface into the liquid.

As shown in Figure 9d, we can see that the cylindrical hollow crystal has a smooth surface, indicating that it is a completely hollow crystal. Surprisingly, when the hollow crystal reached the gas−water meniscus at the left side, a new hollow crystal which is in fact integrated with the hollow crystal in the right side occurs in the gas−water meniscus in the left side (see in Figure 9e). We believe that the growth process of the hollow crystal represents the hydrate bridging effect, and the diagram concerning on the hollow hydrate crystal growth between the adjacent gas phase in the microcapillary is shown in Figure 9f. According to the Yang−Laplace equation, the gas−water interface exhibits a form of meniscus shape because the gas-phase pressure (P_g) is greater than the liquid-phase pressure (P_l). We speculate that the formation of hydrates at the gas−water meniscus reduces the contact surface area of the gas−water interface, causing the molecules to become more crowded with each other and resulting in an increase in the pressure difference between the gas−water phases, forcing the hydrate shell to tend to grow into the liquid phase. Additionally, the hydrate film adsorbs gases under interfacial
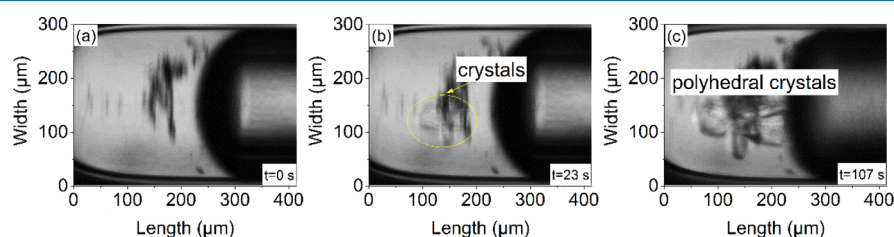

Figure 7. Floating H_2S hydrate crystals at ΔT_{sub} = 3.9 °C. (a) Unnucleated images; (b) hydrate formation in water; and (c) polyhedral crystals evolved from hydrates.
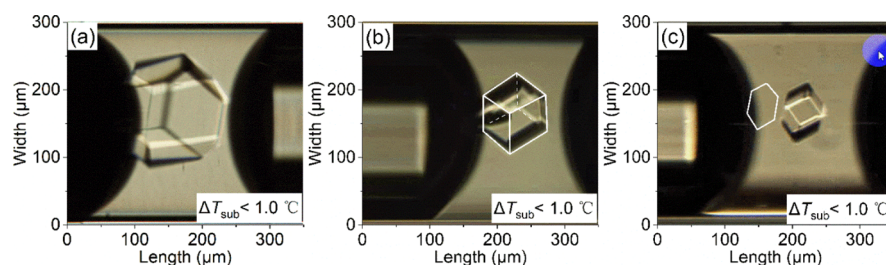
Figure 8. H$_2$S hydrate crystals with different crystalline morphologies under low supercooling conditions: (a) polyhedral crystal; (b) cubic crystal; and (c) hexagonal crystal.
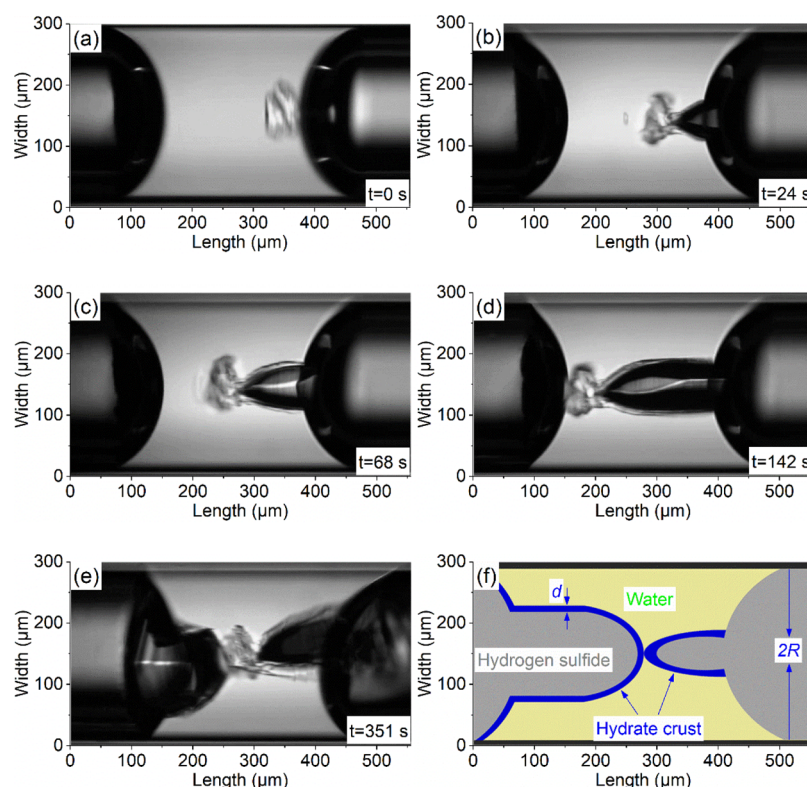

Figure 9. Hollow hydrate crystal growth between the adjacent gas phase in the microcapillary silica tube at ΔT_{sub} = 0.5 °C: (a) hydrate seed at the gas−water meniscus; (b) hollow hydrate at gas−water meniscus; (c) growth of hollow hydrate crystals; (d) hollow hydrate connecting with two sides of the gas phase; (e) new hollow hydrate formation; and (f) schematic diagram of the hollow hydrate crystal growth process.

tension and forms slowly coarsening and thickening hollow crystals during annealing.

The average growth rates of the hydrogen sulfide hydrate in the microcapillary silica tube are given in Figure 10, including
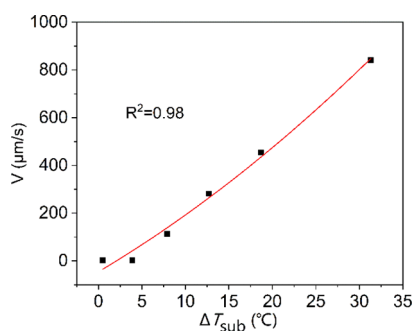

Figure 10. Average growth rate of the H$_2$S hydrate (V in μm/s) vs supercooling degree (ΔT_{sub}).

840, 454, 281, 113, 3.1, and 1.7 μm/s. The dependence of the growth rate of the hydrogen sulfide hydrate on supercooling temperature is shown in eq 5

$$V = -45.4985 + 21.5612 \times \Delta T_{sub} + 0.2223 \times \Delta T_{sub}^2$$

$$R^2 = 0.98 \tag{5}$$

where V is the growth rate of the gas hydrate, μm/s. The empirical equation is not universally applicable. Comparing the growth rate of the hydrogen sulfide hydrate at different supercooling temperatures, it can be seen that the growth rate of the hydrogen sulfide hydrate increases with the increase in supercooling temperatures.

3. CONCLUSIONS

In this study, we applied microcapillary silica tubes to simulate the formation and growth characteristics of gas hydrates in sediment pores. The Raman spectra of different hydrogen sulfide phases were provided in this study, and the Raman shift at 2604 and 2593 cm^{-1} was attributed to S−H stretching

vibrations of H_2S in the small cage (5^{12}) and large cage ($5^{12}6^2$) of the H_2S hydrate, respectively. The measurements and dissociation enthalpies were provided to assess the effect of the microcapillary silica tube size on hydrogen sulfide hydrate dissociation conditions. The dissociation temperature depression of the hydrate crystal in the microcapillary was less than 0.001 °C, which shows that the stability of the hydrate is less affected by the microcapillary pore used in this study.

We have reported the hydrogen sulfide hydrate growth process and morphology at different supercooling temperatures. The experimental results show that the gas hydrate may be formed in fibrous, needle-like crystals and dendrite-like crystals at $\Delta T_{sub} > 12.7$ °C, and dendrite-like crystals and columnar crystals form at $\Delta T_{sub} = 7.9-8.9$ °C, as well as polyhedral crystals at $\Delta T_{sub} < 3.9$ °C. It can be found that the growth rate of the hydrogen sulfide hydrate increases with the increase in supercooling temperatures. The growth of hydrate crystals is greatly affected by mass transfer. The mass transfer from the gas phase to the liquid phase is blocked when the hydrogen sulfide hydrate shell covers the gas–water meniscus, causing the growth of the gas hydrate to be inhibited. Furthermore, a new "bridging effect" that connects with two separated gas phases in a hollow crystal form was found at low supercooling temperature.

4. MATERIALS AND METHODS

4.1. Materials and Apparatus. The experimental setup is shown in Figure 11, and the purities and suppliers of the
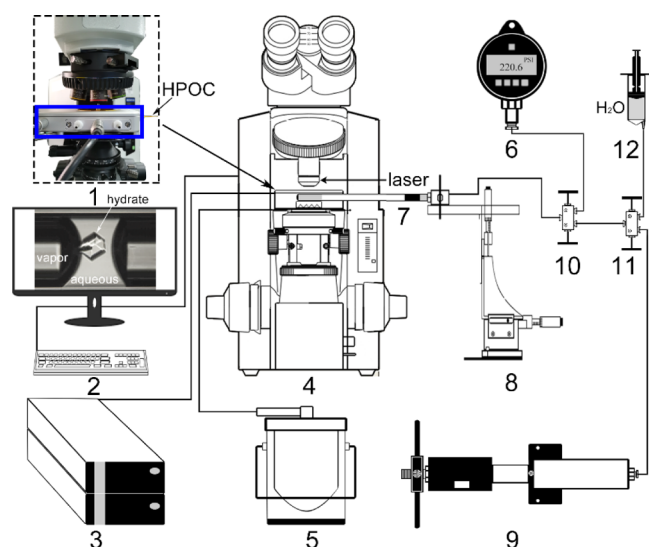

Figure 11. Apparatus for observing H_2S hydrate formation. (1) Heating–cooling stage (blue box); (2) desktop computer; and (3) temperature controller; (4) microscope with a Raman spectrometer; (5) liquid N_2 dewar; (6) pressure transducer; (7) high-pressure optical cell; (9) pressure generator; (10,11) high-pressure valves; and (12) syringe with distilled water.

experimental media (deionized water, hydrogen sulfide, and liquid mercury) are listed in Table 2. A Chou–Burruss–Lu high-pressure optical cell (HPOC), a kind of transparent microcapillary silica tube (Polymicro Technologies Co, Ltd., American) which can withstand pressures more than 80 MPa, was regarded as a reactant cell for hydrate formation.[41,42] The inner diameter (ID), outer diameter (OD), and length of the experimental silica tube were 300 μm, 665 μm, and 24 cm,

Table 2. Suppliers and Purities of the Materials

material	supplier	purity
distilled deionized water	Sichuan Ulupure Technology Co., Ltd	18.25 MΩ·cm
hydrogen sulphide	Wuhan Newradar Special Gas Co., Ltd	99.99 mol %
mercury	Shanghai Macklin Biochemical Co., Ltd	99.9 wt %

respectively (see Figure S1 in the Supporting Information). The capillary silica tube was filled with 20 cm of deionized water, and one of its ends was sealed by hydrogen flame. The deionized water was then displaced to the sealed end of the capillary tube by centrifugation. The open end of the capillary silica tube was inserted into a stainless-steel tube with an approximate outside diameter of 4 cm (1/16 in.) and was glued with the adhesive. As H_2S is highly toxic, the sample containing H_2S–water in the silica tube was sealed with mercury, see the Supporting Information on how to inject H_2S–water and liquid mercury into the silica tube. The sealed end of the capillary silica tube was placed on a silver block in a Linkam CAP500 heating–cooling stage, and the temperature was increased and lowered using a Likam T95 temperature controller and a PE95 nitrogen pump. The temperature was measured using a platinum sensor (± 0.1 °C) placed in a silver block, and its accuracy was periodically checked by monitoring the melting point of the ice. Deionized water was supplied from a pressure generator (HIP Co, Ltd., American) through a stainless-steel line. The system pressure was measured using a digital pressure transducer (Setra Co, Ltd., American). The hydrate formation and decomposition processes were observed with computer software and a microscope. Please see our previously published literature for information on how to prepare the HPOC sample.[18,26,43]

4.2. Procedure. All experiments were conducted under constant pressure with a cooling rate of 5 or 10 °C/min. As the solubility of the gas increases with decreasing temperature, the movement of the gas–water meniscus was observable during the annealing process, and then, the hydrate formation process may occur at the gas–water meniscus. Next, the capillary silica tube was heated at 5 or 10 °C/min to observe the decomposition process of the formed hydrate. The experimental procedure is shown in Figure 12.

As shown in Figure 12a, the temperature and pressure should be fixed to keep the system under a stable condition. Next, keeping the pressure constant, the system temperature is lowered from ambient temperature to T_{ex}. When the system temperature has been cooled to T_{ex}, the hydrate may form on both sides of the gas–water meniscus over a period of time, as shown in Figure 12b. When the hydrogen sulfide hydrate is formed at the gas–water meniscus, the temperature is gradually heated to T_h. When the temperature increases from T_{ex} to T_n ($T_n < T_{eq}$), the gas hydrate crystals will undergo coarse graining, which is typical of Oswald ripening, as shown in Figure 12c. When the system temperature has been increased to T_h ($T_h > T_{eq}$), dissociation of the hydrate crystals will continually occur, as given in Figure 12d. To facilitate the observation, we obtained isolated hydrate crystals by repeated heating and cooling operations, as shown in Figure 12e. Finally, the dissociation conditions of isolated gas hydrates were determined by adjusting the temperature at constant pressure. We provide a video to show the process of hydrate dissociation (see in Videos S4 and S5). Table 3 lists the
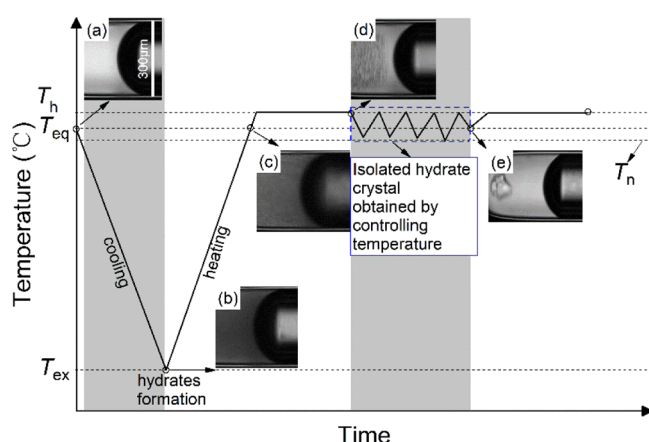
Figure 12. Experimental temperature profile of hydrogen sulfide hydrate formation and dissociation (the size order: $T_h > T_{eq} > T_n \geq T_{ex}$), (a) initial state, (b) hydrate formation, (c) state of the hydrate during the heating process, (d) hydrate dissolved process, and (e) isolated hydrate crystal.

thermodynamic experiments of H_2S hydrate formation in this study.

Table 3. Thermodynamic Experiments of Hydrogen Sulfide Hydrate Formation

experiment	P (psi)	T_{eq} (°C)	T_{ex} (°C)	ΔT_{sub} (°C)
1-1	247.9	27.4	−5.0	32.4
2-1	90.5	18.3	−13.0	31.3
3-1	58.2	13.9	5.0	8.9
3-2	58.2	13.9	6.0	7.9
3-3	58.2	13.9	10.0	3.9
4-1	32.5	7.7	−11.0	18.7
4-2	32.5	7.7	−5.0	12.7
5-1	29.9	7.0	6.5	0.5
6-1				<1.0
6-2	76.4	16.0	15.4	0.6

4.3. Raman Spectroscopy Analysis. As a complement to optical microscopy, laser Raman spectroscopy can provide in situ information on the properties and composition of substances. In this study, Raman spectra of the hydrogen sulfide hydrate at different locations in the capillary were obtained using JY/Horiba LabRam HR Evolution micro confocal Raman spectroscopy. The spectrometer uses a Nd/YAG laser with an excitation wavelength of 532 nm and an output power of 100 mW. The output power of the lens was measured as approximately 14 mW. The Raman spectra were acquired through a 50× telephoto objective with a grating of 1800 scintillations/mm, a micrometer-level spatial resolution, and a spectral resolution of 0.2 cm^{-1}. Before the experiment, peak calibration was using a single silicon (520.7 cm^{-1}). The integration time for spectral acquisition was set to 3−100 s, and the cumulative number of spectral scans was set to 2. The acquired Raman spectra were processed using PeakFit software.

ASSOCIATED CONTENT

Ⓢⓘ Supporting Information

The Supporting Information is available free of charge at https://pubs.acs.org/doi/10.1021/acsomega.1c01051.

Diagram of the HPOC; apparatus diagram for loading H_2S gas in the HPOC; and sample observed in the HPOC with a microscope (20×) (PDF)

Hydrate crystallizes in the dendritic form under strong subcooling conditions (ΔT_{sub} = 15.7 °C) (MP4)

When the ΔT_{sub} was equal to 7.9 °C, we observed a phenomenon in experiment 3-2 that the hydrogen sulfide hydrate formed at the substrate of the micro-capillary (MP4)

Hollow hydrate crystal growth between the adjacent gas phase in the capillary silica tube under low subcooling conditions (ΔT_{sub} = 0.5 °C) (MP4)

Process of hydrate dissociation 1 (MP4)

Process of hydrate dissociation 2 (MP4)

AUTHOR INFORMATION

Corresponding Author

Lei Jiang − *CAS Key Laboratory of Experimental Study Under Deep-Sea Extreme Conditions, Institute of Deep-Sea Science and Engineering, Chinese Academy of Sciences, Sanya, Hainan 572000, China;* ⓄⓇⒸⒾⒹ orcid.org/0000-0002-6901-0480; Email: jl@idsse.ac.cn

Authors

Jiyue Sun − *CAS Key Laboratory of Experimental Study Under Deep-Sea Extreme Conditions, Institute of Deep-Sea Science and Engineering, Chinese Academy of Sciences, Sanya, Hainan 572000, China; University of Chinese Academy of Sciences, Beijing 100049, China*

I-Ming Chou − *CAS Key Laboratory of Experimental Study Under Deep-Sea Extreme Conditions, Institute of Deep-Sea Science and Engineering, Chinese Academy of Sciences, Sanya, Hainan 572000, China;* ⓄⓇⒸⒾⒹ orcid.org/0000-0001-5233-6479

Juezhi Lin − *CAS Key Laboratory of Experimental Study Under Deep-Sea Extreme Conditions, Institute of Deep-Sea Science and Engineering, Chinese Academy of Sciences, Sanya, Hainan 572000, China*

Rui Sun − *Department of Geology, Northwest University, Xi'an 710069, China*

Complete contact information is available at:
https://pubs.acs.org/10.1021/acsomega.1c01051

Notes
The authors declare no competing financial interest.

REFERENCES

(1) Sloan, E. D.; Koh, C. A. *Clathrate Hydrates of Natural Gases*; CRC Press, 2007.

(2) Sloan, D.; Creek, J.; Sum, A. K. Chapter Two—Where and How Are Hydrate Plugs Formed?. In *Natural Gas Hydrates in Flow Assurance*; Sloan, D., Koh, C., Sum, K., Ballard, L., Creek, J., Eaton, M., Lachance, J., McMullen, N., Palermo, T., Shoup, G., Talley, L., Eds.; Gulf Professional Publishing: Boston, 2011; pp 13−36.

(3) Lu, Y.-Y.; Ge, B.-B.; Zhong, D.-L. Investigation of using graphite nanofluids to promote methane hydrate formation: Application to solidified natural gas storage. *Energy* **2020**, *199*, 117424.

(4) Kamata, Y.; Yamakoshi, Y.; Ebinuma, T.; Oyama, H.; Shimada, W.; Narita, H. Hydrogen Sulfide Separation Using Tetra-n-butyl Ammonium Bromide Semi-clathrate (TBAB) Hydrate. *Energy Fuels* **2005**, *19*, 1717−1722.

(5) Wang, X.; Dennis, M.; Hou, L. Clathrate hydrate technology for cold storage in air conditioning systems. *Renewable Sustainable Energy Rev.* **2014**, *36*, 34−51.

(6) Lund, A. Comments to Some Preliminary Results from the Exxon Hydrate Flow Loop. *Ann. N.Y. Acad. Sci.* **1994**, *715*, 447−449.

(7) Kashchiev, D.; Firoozabadi, A. Driving force for crystallization of gas hydrates. *J. Cryst. Growth* **2002**, *241*, 220−230.

(8) Beltrán, J. G.; Servio, P. Morphological Investigations of Methane−Hydrate Films Formed on a Glass Surface. *Cryst. Growth Des.* **2010**, *10*, 4339−4347.

(9) Touil, A.; Broseta, D.; Hobeika, N.; Brown, R. Roles of Wettability and Supercooling in the Spreading of Cyclopentane Hydrate over a Substrate. *Langmuir* **2017**, *33*, 10965−10977.

(10) Nguyen, N. N.; Nguyen, A. V.; Steel, K. M.; Dang, L. X.; Galib, M. Interfacial Gas Enrichment at Hydrophobic Surfaces and the Origin of Promotion of Gas Hydrate Formation by Hydrophobic Solid Particles. *J. Phys. Chem. C* **2017**, *121*, 3830−3840.

(11) Nguyen, N. N.; Galib, M.; Nguyen, A. V. Critical Review on Gas Hydrate Formation at Solid Surfaces and in Confined Spaces— Why and How Does Interfacial Regime Matter? *Energy Fuels* **2020**, *34*, 6751−6760.

(12) Park, T.; Lee, J. Y.; Kwon, T.-H. Effect of Pore Size Distribution on Dissociation Temperature Depression and Phase Boundary Shift of Gas Hydrate in Various Fine-Grained Sediments. *Energy Fuels* **2018**, *32*, 5321−5330.

(13) Fan, S.; Yang, L.; Wang, Y.; Lang, X.; Wen, Y.; Lou, X. Rapid and high capacity methane storage in clathrate hydrates using surfactant dry solution. *Chem. Eng. Sci.* **2014**, *106*, 53−59.

(14) Farhang, F.; Nguyen, A. V.; Sewell, K. B. Fundamental Investigation of the Effects of Hydrophobic Fumed Silica on the Formation of Carbon Dioxide Gas Hydrates. *Energy Fuels* **2014**, *28*, 7025−7037.

(15) Adamova, T. P.; Stoporev, A. S.; Manakov, A. Y. Visual Studies of Methane Hydrate Formation on the Water−Oil Boundaries. *Cryst. Growth Des.* **2018**, *18*, 6713−6722.

(16) Matsuura, R.; Horii, S.; Alavi, S.; Ohmura, R. Diversity in Crystal Growth Dynamics and Crystal Morphology of Structure-H Hydrate. *Cryst. Growth Des.* **2019**, *19*, 6398−6404.

(17) Touil, A.; Broseta, D.; Desmedt, A. Gas Hydrate Crystallization in Thin Glass Capillaries: Roles of Supercooling and Wettability. *Langmuir* **2019**, *35*, 12569−12581.

(18) Jiang, L.; Xin, Y.; Chou, I.-M.; Chen, Y. Raman spectroscopic measurements of ν1 band of hydrogen sulfide over a wide range of temperature and density in fused-silica optical cells. *J. Raman Spectrosc.* **2018**, *49*, 343−350.

(19) Salmoun, F.; Dubessy, J.; Garrabos, Y.; Marsault-Herail, F. Raman spectra of H2S along the liquid−vapour coexistence curve. *J. Raman Spectrosc.* **1994**, *25*, 281−287.

(20) Chazallon, B.; Focsa, C.; Charlou, J.-L.; Bourry, C.; Donval, J.-P. A comparative Raman spectroscopic study of natural gas hydrates collected at different geological sites. *Chem. Geol.* **2007**, *244*, 175−185.

(21) Lee, S.; Seo, Y. Experimental Measurement and Thermodynamic Modeling of the Mixed CH4 + C3H8 Clathrate Hydrate Equilibria in Silica Gel Pores: Effects of Pore Size and Salinity. *Langmuir* **2010**, *26*, 9742−9748.

(22) Mekala, P.; Babu, P.; Sangwai, J. S.; Linga, P. Formation and Dissociation Kinetics of Methane Hydrates in Seawater and Silica Sand. *Energy Fuels* **2014**, *28*, 2708−2716.

(23) Sun, Q.; Du, M.; Li, X.; Guo, X.; Liu, A.; Chen, G.; Yang, L. Study on ethane hydrate formation/dissociation in a sub-millimeter sized capillary. *Chem. Eng. Sci.* **2019**, *206*, 1−9.

(24) Martinez de Baños, M. L.; Carrier, O.; Bouriat, P.; Broseta, D. Droplet-based millifluidics as a new tool to investigate hydrate

crystallization: Insights into the memory effect. *Chem. Eng. Sci.* **2015**, *123*, 564−572.

(25) Sakemoto, R.; Sakamoto, H.; Shiraiwa, K.; Ohmura, R.; Uchida, T. Clathrate Hydrate Crystal Growth at the Seawater/Hydrophobic− Guest−Liquid Interface. *Cryst. Growth Des.* **2010**, *10*, 1296−1300.

(26) Sun, J.; Xin, Y.; Chou, I. M.; Sun, R.; Jiang, L. Hydrate Stability in the H2S−H2O system—Visual Observations and Measurements in a High-Pressure Optical Cell and Thermodynamic Models. *J. Chem. Eng. Data* **2020**, *65*, 3884−3892.

(27) Adeniyi, K. I.; Deering, C. E.; Nagabhushana, G. P.; Marriott, R. A. Hydrogen Sulfide Hydrate Dissociation in the Presence of Liquid Water. *Ind. Eng. Chem. Res.* **2018**, *57*, 15579−15585.

(28) Kvamme, B.; Coffin, R. B.; Zhao, J.; Wei, N.; Zhou, S.; Li, Q.; Saeidi, N.; Chien, Y.-C.; Dunn-Rankin, D.; Sun, W.; Zarifi, M. Stages in the Dynamics of Hydrate Formation and Consequences for Design of Experiments for Hydrate Formation in Sediments. *Energies* **2019**, *12*, 3399.

(29) Kvamme, B.; Zhao, J.; Wei, N.; Sun, W.; Zarifi, M.; Saeidi, N.; Zhou, S.; Kuznetsova, T.; Li, Q. Why Should We Use Residual Thermodynamics for Calculation of Hydrate Phase Transitions? *Energies* **2020**, *13*, 4135.

(30) Clennell, M. B.; Hovland, M.; Booth, J. S.; Henry, P.; Winters, W. J. Formation of natural gas hydrates in marine sediments: 1. Conceptual model of gas hydrate growth conditioned by host sediment properties. *J. Geophys. Res.: Solid Earth* **1999**, *104*, 22985− 23003.

(31) Duan, Z.; Li, D.; Chen, Y.; Sun, R. The influence of temperature, pressure, salinity and capillary force on the formation of methane hydrate. *Geosci. Front.* **2011**, *2*, 125−135.

(32) Carroll, J. *Natural Gas Hydrates: A Guide for Engineers*, 2nd ed.; Elsevier, 2009.

(33) Duan, Z.; Sun, R.; Liu, R.; Zhu, C. Accurate Thermodynamic Model for the Calculation of H2S Solubility in Pure Water and Brines. *Energy Fuels* **2007**, *21*, 2056−2065.

(34) Kvamme, B.; Zhao, J.; Wei, N.; Sun, W.; Saeidi, N.; Pei, J.; Kuznetsova, T. Hydrate Production Philosophy and Thermodynamic Calculations. *Energies* **2020**, *13*, 672.

(35) Zeng, X.-Y.; Wu, G.; Zhong, J.-R.; Chen, D.-Y.; Sun, C.-Y.; Chen, G.-J. Three-Scale in Situ Investigation on the Film Morphology and Mass Transfer Channels during the Thickening Growth of Hydrates on Gas Bubble. *Cryst. Growth Des.* **2019**, *19*, 3158−3165.

(36) Ohmura, R.; Shimada, W.; Uchida, T.; Mori, Y. H.; Takeya, S.; Nagao, J.; Minagawa, H.; Ebinuma, T.; Narita, H. Clathrate hydrate crystal growth in liquid water saturated with a hydrate-forming substance: variations in crystal morphology. *Philos. Mag.* **2004**, *84*, 1− 16.

(37) Ohmura, R.; Matsuda, S.; Uchida, T.; Ebinuma, T.; Narita, H. Clathrate Hydrate Crystal Growth in Liquid Water Saturated with a Guest Substance: Observations in a Methane + Water System. *Cryst. Growth Des.* **2005**, *5*, 953−957.

(38) Kuang, Y.; Feng, Y.; Yang, L.; Song, Y.; Zhao, J. Effects of Micro-bubbles on the Nucleation and Morphology of the Gas Hydrate Crystals. *Phys. Chem. Chem. Phys.* **2019**, *21*, 23401.

(39) Jin, Y.; Nagao, J. Morphological Change in Structure H Clathrates of Methane and Liquid Hydrocarbon at the Liquid−Liquid Interface. *Cryst. Growth Des.* **2011**, *11*, 3149−3152.

(40) Karanjkar, P. U.; Lee, J. W.; Morris, J. F. Surfactant Effects on Hydrate Crystallization at the Water−Oil Interface: Hollow-Conical Crystals. *Cryst. Growth Des.* **2012**, *12*, 3817−3824.

(41) Chou, I.-M.; Burruss, R. C.; Lu, W., Chapter 24—A new optical capillary cell for spectroscopic studies of geologic fluids at pressures up to 100 MPa. In *Advances in High-Pressure Technology for Geophysical Applications*; Chen, J., Wang, Y., Duffy, T. S., Shen, G., Dobrzhinetskaya, L. F., Eds.; Elsevier: Amsterdam, 2005; pp 475− 485.

(42) Chou, I.-M.; Song, Y.; Burruss, R. C. A new method for synthesizing fluid inclusions in fused silica capillaries containing organic and inorganic material. *Geochim. Cosmochim. Acta* **2008**, *72*, 5217−5231.

(43) Jiang, L.; Xin, Y.; Chou, I.-M.; Sun, R. Raman spectroscopic measurements of H2S solubility in pure water over a wide range of pressure and temperature and a refined thermodynamic model. *Chem. Geol.* **2020**, *555*, 119816.